

Euler-Euler Simulation of Absorption and Desorption in Co- and Counter-current Bubble Column Flows

Khan, H.; Lehnigk, R.; Rzehak, R.;

Originally published:

November 2022

Chemical Engineering Science 267(2023), 118313

DOI: <https://doi.org/10.1016/j.ces.2022.118313>

Perma-Link to Publication Repository of HZDR:

<https://www.hzdr.de/publications/Publ-35574>

Release of the secondary publication
on the basis of the German Copyright Law § 38 Section 4.

CC BY-NC-ND

1 Euler-Euler Simulation of Absorption and Desorption
2 in Co- and Counter-current Bubble Column Flows

3
4 Haris Khan*, Ronald Lehnigk, Roland Rzehak

5
6
7 Helmholtz-Zentrum Dresden – Rossendorf, Institute of Fluid Dynamics,
8 Bautzner Landstrasse 400, D-01328 Dresden, Germany

9
10
11 **Abstract**

12 Mass transfer in bubbly flows is important in many engineering applications. Simulation of
13 such processes on technical scales is feasible by the Euler-Euler two-fluid model, which relies
14 on suitable closure relations describing interfacial exchange processes. In comparison with
15 the pure fluid dynamics of bubbly flows however, modeling and simulation of bubbly flows
16 including mass transfer is significantly less developed. In particular, previous studies have
17 focused entirely on absorption in upward vertical flows, whereas the present study considers
18 a larger variety of conditions including desorption and counter-current (downward) flow.
19 Suitable experimental data for comparison are available from the classic work of Deckwer et
20 al. [*Canadian Journal of Chemical Engineering* 56 (1978) 43-55]. In line with previous studies
21 on the co-current absorption cases from that work, a monodisperse approximation is made.
22 In addition, a class method to treat bubble shrinkage and growth is implemented in the
23 OpenFOAM code and tested by showing the crossover between two monodisperse cases.

24
25 **Keywords:** mass-transfer, dispersed gas-liquid multiphase flow, Euler-Euler two-fluid model,
26 closure relations, CFD simulation, model validation

27
28

* Corresponding author. E-mail: h.khan@hzdr.de

29 1 INTRODUCTION

30 Transfer of mass between gas bubbles and the liquid around them is an important
31 consideration in different branches of chemical and process engineering. Simulation of such
32 processes on the scale of technical equipment is feasible by the Euler-Euler two-fluid model,
33 which requires closure relations describing the interfacial exchange of mass and momentum.
34 Concerning pure fluid dynamics of dispersed gas-liquid multiphase flow, an ongoing effort has
35 led to a validated set of closures that is applicable under a rather broad range of conditions.
36 However, similar results for the technologically even more important field of mass transfer
37 yet remain to be achieved. This is evidenced by the still rather limited number of studies
38 considering mass exchange either without or with an accompanying chemical reaction.

39 Earlier work in this field has been reviewed in Rzehak and Krepper (2016) for mass-transfer
40 without reaction and in Krauß and Rzehak (2018, 2017) for mass-transfer with an
41 accompanying reaction. Since then, the topic has received continued high interest in both
42 experimental (Kipping et al. 2020, Kovats et al. 2018) and simulation studies by the Euler-Euler
43 and Euler-Lagrange methods (Taborda and Sommerfeld 2021, Hlawitschka et al. 2017b). In all
44 of these investigations, the focus was put on reactive systems such as CO₂ in aqueous NaOH
45 (Hori et al. 2020) or NO in aqueous FeII complexes (Hlawitschka et al. 2017a). Applied models
46 for the mass transfer correlations in these works range from simple correlations in terms of
47 powers of the Reynolds and Schmidt number in Hlawitschka et al. (2017b) to elaborate
48 models taking into account bubble oscillations in Taborda and Sommerfeld (2021). From the
49 overview of Solsvik (2018) it may be concluded that the search for a model for the bubbles'
50 mass transfer coefficient that is both well-validated and broadly applicable remains ongoing
51 despite these recent advances. One particular limitation of all previous works is the exclusive
52 focus on absorption in upward vertical flows.

53 A first step is taken here towards more general configurations including desorption and
54 counter-current (downward) flow in Euler-Euler simulations using the open-source software
55 OpenFOAM. To this end, experimental data for comparison are available from the work of
56 Deckwer et al. (1978). Cases from this work concerning absorption in co-current (upward)
57 flow have been considered previously by performing simulations in ANSYS CFX (Rzehak and
58 Krepper 2016). As noted there, a peculiarity of this data set is that despite the mass transfer,
59 the mean bubble size did not change for the set of conditions where measurements of this
60 quantity were taken at different heights. Since the bubbles lose a significant amount of mass
61 due to the absorption, it was suggested already by Deckwer et al. (1978) that this must be
62 attributed to the simultaneous occurrence of coalescence between them.

63 Based on this finding it is possible to treat the bubble size distribution as monodisperse using
64 the measured average size d_B . This bypasses the additional complexity of modeling bubble
65 coalescence and breakup processes, but on the other hand a size dependence of the mass
66 transfer coefficient k_L cannot be resolved. Therefore, the experimentally determined values
67 for k_L are substituted here in accordance with the previous works. As it will turn out, a
68 reasonable agreement with the experiments can nonetheless be obtained.

69 Finally, bubble shrinkage and growth are considered within a framework for polydisperse
70 bubbly flow based on the population balance equation. A class method has recently been
71 implemented into OpenFOAM for this purpose (Lehnigk 2020, Lehnigk et al. 2022). Presently,
72 the necessary source terms describing bubble shrinkage and growth are added to this
73 implementation based on a simple upwind discretization (OpenFOAM Foundation 2021). A
74 demonstration of the method is given showing the crossover between two monodisperse

75 cases. A full validation requires measurements of the bubble size distribution at different
 76 levels in the column and hence has to await further investigation.

77 The remainder of the paper is organized as follows. A summary of the selected test cases
 78 including various configurations with absorption and desorption as well as co- and counter-
 79 current flow is given in section 2. The modeling of mass transfer for both monodisperse and
 80 polydisperse cases is described in section 3. The simulation results are presented in section 4
 81 and compared to the available measurements as well as previous simulation results obtained
 82 using ANSYS CFX. A discussion is given in section 5.

83

84 2 SUMMARY OF EXPERIMENTAL DATA

85 The work of Deckwer et al. (1978) investigated mass transfer in bubble columns as sketched
 86 in Figure 1. Several different configurations were studied. For co-current flow, the liquid
 87 entered the test section within the column at the bottom and flowed upwards together with
 88 the gas. For counter-current flow in contrast, the liquid entered the test section at the top
 89 and flowed downwards in opposition to the gas. For absorption, the transferred species was
 90 supplied mainly together with the gas, while for desorption, it was supplied mainly with the
 91 liquid. A smaller preloading of the other phase was applied in some cases as well.

92 Two bubble columns were used differing in size and equipped with different gas distributors.
 93 For bubble column BC I, the column diameter was $D = 200$ mm while its height was $H = 7200$
 94 mm $\approx 36 D$. A cross-shaped sparger with 1 mm holes was used. For bubble column BC II, the
 95 column diameter was $D = 150$ mm while its height was $H = 4400$ mm $\approx 30 D$. A porous plate
 96 sparger with 150 μm pores was used. The porous plate was circular in shape with a diameter
 97 of 140 mm (Burkhart 1976), leaving a circular ring of 5 mm width for the liquid to pass
 98 through.

99

100 Table 1: Parameters for the selected tests from Deckwer et al. (1978).

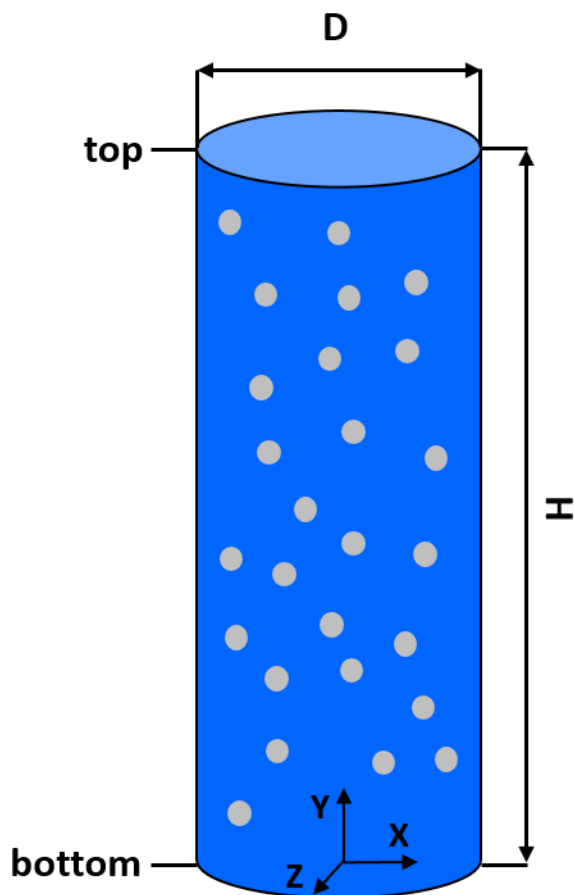
test	16	W23	W13	W15	W3
configuration	co. abs.	co. abs.	counter. abs.	counter. abs.	counter. des.
geometry	BC II	BC I	BC I	BC I	BC I
$J_G (bot)$ [m/s]	0.0275	0.0261	0.0144	0.0196	0.0155
$J_L (bot)$ [m/s]	0.0472	0.0265	0.0265	0.0265	0.0265
$\alpha_G (bot)$ [m^3/m^3]	0.060	0.052	0.050	0.064	0.052
$Y_G^{CO_2} (bot)$ [kg/kg]	0.885	0.493	0.818	0.660	0
$Y_L^{CO_2} (bot)$ [kg/kg]	0	0	-	-	-
$Y_L^{CO_2} (top)$ [kg/kg]	-	-	0.300e-3	0.285e-3	1.43e-3
d_B [mm]	2.9	2.9	2.9	2.9	2.9
k_L [mm/s]	0.21	0.0906	0.0891	0.0935	0.0578

101

102 CO₂ was used as the transferred species and the bubbles consisted of a mixture of CO₂ and
103 air, while the liquid was water. A temperature of 14°C was maintained during the experiments
104 and the top of the column was at ambient pressure. Parameters varied for each test comprise
105 the gas and liquid fluxes as well as the initial CO₂ content of the phases.

106 The measurements provide steady state axial profiles of gas fraction and CO₂ content in the
107 bubbles or the liquid. For the present work, tests have been selected where measurements
108 of both gas fraction and CO₂ content are available. Effective values of the mass transfer
109 coefficient were determined from the measured concentrations. An average bubble size is
110 reported as well, which as already explained was found constant despite the mass transfer.
111 The relevant parameters of the selected test cases are summarized in Table 1. While the
112 volumetric fluxes J_G and J_L as well as the concentrations $Y_G^{CO_2}$ and $Y_L^{CO_2}$ at the respective
113 locations were directly reported for the experiment, the inlet gas fraction at the column
114 bottom was determined by fitting a parabola to the measured axial profiles.

115



116

117

118 Figure 1: Geometry for the test section within the bubble columns from Deckwer et al. (1978).

119

120 3 DESCRIPTION OF PHYSICAL MODELS

121 This section describes the physical models used for the simulations. For the sake of clarity, a
 122 monodisperse situation is considered first in section 3.1 on the part concerned with mass
 123 transfer and in section 3.2 on the fluid dynamical part of the model. The latter closely follows
 124 a baseline approach validated in a number of previous studies, and hence, only a concise
 125 summary is offered together with references on the original works. The extension of the
 126 model for polydisperse flows is covered in section 3.3. Finally, in section 3.4, other aspects of
 127 the model are summarized like material properties, geometric simplifications and boundary
 128 conditions.

129 3.1 Mass Transfer

130 Mass transfer is described by separate mass balances for the transferred species in addition
 131 to the total mass balances expressed by the continuity equations (see section 3.2) for each
 132 phase. Denoting the transferred species as A , these equations read

$$\frac{\partial}{\partial t}(\alpha_G \rho_G Y_G^A) + \nabla \cdot (\alpha_G \rho_G \mathbf{u}_G Y_G^A) = \nabla \cdot (\alpha_G \rho_G D_G^{eff,A} \nabla Y_G^A) + \Gamma_G^A \quad (1)$$

$$\frac{\partial}{\partial t}(\alpha_L \rho_L Y_L^A) + \nabla \cdot (\alpha_L \rho_L \mathbf{u}_L Y_L^A) = \nabla \cdot (\alpha_L \rho_L D_L^{eff,A} \nabla Y_L^A) + \Gamma_L^A . \quad (2)$$

133 Here, A appears as a solute in each phase and $Y^A = \rho^A / \rho$ represents its mass fraction, which
 134 is expressed in terms of the density $\rho = \sum_X \rho^X$ of the multi-component mixture of which
 135 each phase consists. The mass fraction of the solvent in each phase can be obtained from the
 136 constraint $\sum_X Y^X = 1$. One should carefully distinguish the mass concentration of a species in
 137 a mixture should from the thermodynamic density of the pure substance, despite the
 138 unfortunate convention to use the same letter ρ for both. The phase fraction α and phasic
 139 velocity \mathbf{u} are provided by the solution of the fluid dynamical part of the model. The effective
 140 diffusion coefficient $D^{eff,A}$ and the source terms due to transport across the phase interface
 141 Γ^A have to be modeled as described below.

142 In fluid dynamics the use of mass fractions Y^A is customary, since mass is a conserved
 143 quantity. In chemical engineering in contrast, mole fractions X^A are more commonly used
 144 since the number of particles arises in the formulation of chemical reactions. The mole
 145 fraction is defined analogously to the mass fraction as $X^A = c^A / c$ with $c = \sum_X c^X$, the molar
 146 concentration of the mixture. With the aid of the equivalent relations

$$M = \sum_X X^X M^X \quad ; \quad \frac{1}{M} = \sum_X \frac{Y^X}{M^X} \quad (3)$$

147 for the mixture molar mass M , mass and mole fractions may be converted according to

$$Y^X = \frac{M^X}{M} X^X . \quad (4)$$

148 Hence, the quantities Y^A , X^A , ρ^A , and c^A , all of which are frequently encountered in the
 149 literature on mass transfer, will be used interchangeably from hereon.

150 The source terms Γ^A for both phases, which describe the transport of mass across the
 151 interface, are related as $\Gamma_G^A = -\Gamma_L^A$ as a consequence of species mass conservation. For
 152 absorption $\Gamma_L^A > 0$, while for desorption $\Gamma_L^A < 0$. Since the resistance to mass transfer

153 typically occurs mostly on the liquid side, Γ_L^A is a function of the concentration difference in
 154 the liquid next to the interface and in the bulk liquid. Concentrations in the gas and liquid next
 155 to the interface can be related by Henry's law to arrive at

$$\Gamma_L^A = k_L a_I \rho_L \left(He^A Y_G^A \frac{\rho_G}{\rho_L} - Y_L^A \right). \quad (5)$$

156 Here the interfacial area concentration a_I is

$$a_I = \frac{6\alpha_G}{d_B} \quad (6)$$

157 based on the assumption of spherical bubbles, while the bubble size d_B and mass transfer
 158 coefficient k_L are constants taken from the experiments as discussed in section 2. The Henry
 159 constant He^A and the densities ρ_L and ρ_G are material properties (see section 3.4).

160 Finally, the effective diffusion coefficient for the continuous liquid phase is the sum of
 161 molecular and turbulent contributions D_L^A and $D_L^{turb,A}$. The former is again a material
 162 property while the latter is calculated from the turbulent kinematic viscosity by means of a
 163 turbulent Schmidt number, for which a value of unity is assumed (e.g. Cockx et al. 2001), i.e.

$$Sc_L^{turb} = \frac{\nu_L^{turb}}{D_L^{A,turb}} = 1. \quad (7)$$

164 The turbulent kinematic viscosity ν_L^{turb} is obtained from the turbulence model (see section
 165 3.2). Since no diffusive transport occurs between bubbles, $D_G^A = 0$ for the dispersed gas
 166 phase.

167

168 3.2 Fluid Dynamics

169 The conservation equations for two-phase flow are summarized as follows (e.g. Drew and
 170 Passman 1998, Yeoh and Tu 2010, Ishii and Hibiki 2011).

171 The balance of total mass for each phase is expressed by the phasic continuity equations
 172 which read

$$\frac{\partial}{\partial t}(\alpha_G \rho_G) + \nabla \cdot (\alpha_G \rho_G \mathbf{u}_G) = \Psi_G^A \quad (8)$$

$$\frac{\partial}{\partial t}(\alpha_L \rho_L) + \nabla \cdot (\alpha_L \rho_L \mathbf{u}_L) = \Psi_L^A. \quad (9)$$

173 Likewise the momentum balance for each phase is given by

$$\begin{aligned} \frac{\partial}{\partial t}(\alpha_G \rho_G \mathbf{u}_G) + \nabla \cdot (\alpha_G \rho_G \mathbf{u}_G \otimes \mathbf{u}_G) \\ = -\alpha_G \nabla p_G + \nabla \cdot (\alpha_G \mathbf{T}_G) + \alpha_G \rho_G \mathbf{g} + \mathbf{F}_G^{inter} + \Phi_G^A \end{aligned} \quad (10)$$

$$\begin{aligned} \frac{\partial}{\partial t}(\alpha_L \rho_L \mathbf{u}_L) + \nabla \cdot (\alpha_L \rho_L \mathbf{u}_L \otimes \mathbf{u}_L) \\ = -\alpha_L \nabla p_L + \nabla \cdot (\alpha_L \mathbf{T}_L) + \alpha_L \rho_L \mathbf{g} + \mathbf{F}_L^{inter} + \Phi_L^A. \end{aligned} \quad (11)$$

174 In these equations, the last terms on the right represent sources due to the mass transfer. For
 175 the monodisperse treatment, the sources Ψ^A for the total mass required in the continuity
 176 equations are of course the same as those for the species mass which have already been

177 described in the previous section, i.e. $\Psi^A = \Gamma^A$. The so-called secondary momentum sources
 178 are given by

$$\Phi_G^A = -\mathbf{u}_G \Gamma_L^A \quad \text{for } \Gamma_L^A > 0 \quad (\text{absorption}) \quad (12)$$

$$\Phi_L^A = \mathbf{u}_G \Gamma_L^A \quad (13)$$

$$\Phi_G^A = -\mathbf{u}_L \Gamma_L^A \quad \text{for } \Gamma_L^A < 0 \quad (\text{desorption}) \quad (14)$$

$$\Phi_L^A = \mathbf{u}_L \Gamma_L^A, \quad (15)$$

179 which satisfy $\Phi_G^A = -\Phi_L^A$ as required by conservation of momentum.

180 The terms \mathbf{F}^{inter} describe the transfer of momentum between both phases. The relation
 181 $\mathbf{F}_G^{inter} = -\mathbf{F}_L^{inter}$ holds as a consequence of overall momentum conservation. According to
 182 the baseline model adopted here, these terms are composed of several different
 183 contributions listed in Table 2. The closure correlation which is used for each of these is also
 184 shown in the table. Studies providing further details and validation of this baseline model are
 185 e.g. Ziegenhein et al. (2013), Rzehak et al. (2015), Rzehak and Krepper (2015), or Rzehak et al.
 186 (2017a).

187 In terms of an effective viscosity which comprises both viscous and turbulent contributions
 188 the stress tensor is expressed as

$$\mathbf{T} = \mu^{eff} (\nabla \mathbf{u} + (\nabla \mathbf{u})^T). \quad (16)$$

189 The effective dynamic viscosity μ_L^{eff} is calculated from a k- ω SST model (Menter 2009) for
 190 the liquid phase. For the baseline model, additional source terms are included to take account
 191 of the bubble-induced turbulence (Ma et al. 2017). Turbulence may be neglected for the gas
 192 phase because of the low density and small spatial scales of the bubbles by setting $\mu_G^{eff} = 0$.
 193 Studies providing further details on turbulence modeling in the baseline approach are e.g.
 194 Rzehak and Krepper (2013a), Rzehak and Kriebitzsch (2015), Ziegenhein et al. (2017) or Parekh
 195 and Rzehak (2018).

196 The above system of equations requires two further relations for completion. These are
 197 provided by $\alpha_G + \alpha_L = 1$ expressing the overall conservation of volume and $p_G = p_L = p$
 198 expressing the equilibrium of pressures. Finally both phases are taken to be incompressible.

199

200 Table 2: Summary of bubble force correlations.

force	reference
drag	Ishii and Zuber (1979)
shear lift	Tomiya et al. (2002)
wall lift	Hosokawa et al. (2002)
turbulent dispersion	Burns et al. (2004)
virtual mass	constant coefficient $C_{VM} = \frac{1}{2}$

201

202

203 3.3 Polydispersity

204 A description of polydisperse and evolving bubble size distributions is feasible by means of a
 205 population balance equation (Ramkrishna 2000, Marchisio and Fox 2013 ch 4). Several
 206 approaches to its discretization have been proposed. Among these, a class method (also
 207 known as sectional method or MUSIG model) has recently been implemented in OpenFOAM
 208 v9 (OpenFOAM Foundation 2021, 2021a), which is taken as the basis of the present work.
 209 Two variants of this approach exist, termed the homogeneous one, in which bubbles of all sizes
 210 share the same velocity field and the inhomogeneous one, in which bubbles of different size are
 211 allowed to move with different velocities. Introduction of the latter (Krepper et al. 2008) was
 212 motivated by the fact that the bubbles' lift coefficient changes its sign at a certain bubble size,
 213 (~ 5.8 mm for the presently used correlation of Tomiyama et al. (2002)), which causes different
 214 motion of smaller and larger bubbles. Since in the present applications, the bubbles are of
 215 significantly smaller size, only the simpler homogeneous variant is considered for the purpose to
 216 demonstrate the bubble shrinkage due to absorption.

217 In this approach, the range of bubble sizes is discretized into a finite number of intervals, so-
 218 called size groups, each of which is assigned a representative value of bubble size $d_{B,i}$. A
 219 discrete representation of the bubble size distribution is obtained by the values of the gas
 220 fraction $\alpha_{G,i}$ in each size group $i = 1 \dots M$, for each of which a separate continuity equation
 221 of the same type as Eq. (8) has to be solved, i.e.

$$\frac{\partial}{\partial t} (\alpha_{G,i} \rho_G) + \nabla \cdot (\alpha_{G,i} \rho_G \mathbf{u}_{G,i}) = \Psi_{G,i}^A. \quad (17)$$

222 In addition there are a single momentum balance equation (10) and species balance equation
 223 (1) for the gas phase and a set of equations for the liquid phase, Eqs. (9), (11), (2).
 224 Whenever the bubble size is needed in the momentum or species equations, the mean Sauter
 225 diameter over all size groups is used, namely

$$d_B = \left(\sum_{i=1}^M \frac{\alpha_{G,i}}{\alpha_G} d_{B,i}^{-1} \right)^{-1}, \quad (18)$$

226 For the purpose of calculating the change of bubble size due to absorption or desorption, the
 227 amount of mass transferred to/from the liquid can be calculated for each size group $i = 1 \dots$
 228 M in the same way as for the monodisperse case, i.e.

$$\Gamma_{L,i}^A = k_{L,i} a_{L,i} \rho_L \left(H e^A Y_{G,i}^A \frac{\rho_G}{\rho_L} - Y_L^A \right), \quad (19)$$

229 and the total mass sources in both the continuity and species balance equations for the liquid
 230 are of course

$$\Psi_L^A = \Gamma_L^A = \sum_{i=1}^M \Gamma_{L,i}. \quad (20)$$

231 However, the negative of Eq. (19) does not directly give the source term $\Psi_{G,i}^A$ in the continuity
 232 equation of the i -th size group, since due to the accompanying change in bubble size, mass is
 233 also shifted to the next smaller size group for absorption and the next larger one for
 234 desorption. The derivation is most easily given when the bubble mass is used as the internal
 235 coordinate rather than the bubble size. Both descriptions are related by

$$d_{B,i} = \left(\frac{6 m_{B,i}}{\pi \rho_G} \right)^{1/3}, \quad (21)$$

236 and the final result is readily transformed to the desired expression in terms of the bubble
237 size, which is used as the internal coordinate in the OpenFOAM implementation.

238 The form of these source terms for the continuity equations of each size group is then inferred
239 as follows. If one bubble is shifted from group i to the adjacent group k , where $k = i - 1$ for
240 absorption and $k = i + 1$ for desorption, it changes its mass by an amount of $|m_i - m_k|$. Since
241 the change of mass contained in group i due to absorption to or desorption from the liquid is
242 given by $|\Gamma_{L,i}^A|$ the number of bubbles that must be shifted from group i to k to effect this
243 change can be calculated as $|\Gamma_{L,i}^A|/|m_i - m_k|$. The mass lost or gained in either size group is
244 then obtained by multiplying the number of bubbles shifted between them with the group's
245 representative mass. The difference between both is precisely the amount of mass
246 transferred to / from the liquid. By forcing the change of bubble mass, which in reality takes
247 place continuously in infinitesimal steps, to occur in finite steps proportional to the difference
248 of the group's representative mass results in an upwind-type discretization. The expressions
249 obtained for the source terms are

$$\Psi_{G,i}^A = -\frac{m_i}{m_i - m_{i-1}} \Gamma_{L,i}^A + \frac{m_i}{m_{i+1} - m_i} \Gamma_{L,i+1}^A \quad \text{for } \Gamma_{L,i}^A > 0 \quad (\text{abs.}) \quad (22)$$

$$\Psi_{G,i}^A = -\frac{m_i}{m_i - m_{i-1}} \Gamma_{L,i-1}^A + \frac{m_i}{m_{i+1} - m_i} \Gamma_{L,i}^A \quad \text{for } \Gamma_{L,i}^A < 0 \quad (\text{des.}) \quad (23)$$

250 Note that in the second of these, since $\Gamma_{L,i}^A < 0$ for desorption the first term actually
251 represents a source and the second one a sink. For the smallest group, $i = 1$, we define $m_0 =$
252 0 , which for absorption expresses the fact that the mass loss from the smallest bubbles is only
253 to the liquid. For desorption, we additionally let $\Gamma_{L,0}^A = 0$, which means that no nucleation
254 occurs. For the largest group, $i = M$, care needs to be taken that the gas fraction in this group
255 never becomes non-zero during the simulation, which will make $\Gamma_{L,M}^A = 0$. For absorption this
256 is straight forward to achieve based on the initial bubble size distribution. For desorption,
257 additional prior knowledge is required or the necessary size/mass for the largest group has to
258 be found by trial and error. With these additional settings it may readily be verified from Eqs.
259 (22) and (23) that for both absorption and desorption

$$\sum_{i=1}^M \Psi_{G,i}^A \equiv \Psi_G^A = -\Psi_L^A, \quad (24)$$

260 as required by conservation of total mass.

261 Variations of species concentration in the different size groups can currently not be resolved
262 in OpenFOAM, but the average species concentration of all size groups can be tracked. The
263 source terms for the species mass fraction equations for gas and liquid phase are given by

$$\Gamma_G^A = -\Gamma_L^A = \sum_{i=1}^M \Gamma_{G,i}^A \quad (25)$$

264 as required by species mass conservation. For the secondary sources in the gas phase
265 momentum equation we have

$$\Phi_G^A = -\Phi_L^A = -\mathbf{u}_G \sum_{i=1}^M \Gamma_{L,i}^A \quad \text{for } \Gamma_{L,i}^A > 0 \quad (\text{abs.}) \quad (26)$$

$$\Phi_G^A = -\Phi_L^A = -\mathbf{u}_L \sum_{i=1}^M \Gamma_{L,i}^A \quad \text{for } \Gamma_{L,i}^A < 0 \quad (\text{des.}) \quad (27)$$

266 as required by momentum conservation.

267 As mentioned above, the final result is obtained by transforming all of the equations to a size-
268 based description by means of Eq. (21).

269

270 3.4 Other Model Aspects

271 A set of correlations describing the material properties of mixtures of CO₂ with water was
272 assembled from literature sources by Rzehak and Krepper (2016). For the present work, these
273 correlations are evaluated at the temperature of 14°C corresponding to the experimental
274 conditions. The gas phase is treated as an ideal gas consisting of a mixture of CO₂ and air to
275 take into account the effect of the hydrostatic pressure according to the ideal gas law $\rho_G =$
276 $(p M_G)/(R T)$. The importance of this effect will be highlighted by comparison to an
277 alternative model assuming the gas phase to be incompressible, i.e. taking $\rho_G = \text{const.}$ The
278 liquid phase is considered as incompressible throughout. The values of all relevant material
279 properties are summarized in Table 3.

280

281 Table 3: Relevant material properties of mixtures of CO₂ with water and air at 14 °C.

	Gas		Liquid
	Air	CO ₂	Water
M [g/mol]	29	44	18
ρ [kg/m ³]	1.23	1.85	998
μ [Pa s]	1.79e-05	1.44e-05	1.16e-03
σ [Nm ⁻¹]	-	0.073	
He^{CO_2} [-]	-	1.04	
D^{CO_2} [m ² s ⁻¹]	-	1.46e-09	

282

283 The geometrical setup is chosen in agreement with the previous simulations of Rzehak and
284 Krepper (2016). A quasi-2D domain consisting of a narrow sector of the column is considered,
285 which implies that an axisymmetric flow is assumed. Meshes with the same radial resolution
286 as in Rzehak and Krepper (2016) were used while the axial resolution was increased by a factor
287 of 1.5 to improve the results near the inlet. The imposed boundary conditions depend on the
288 configuration, i.e. whether the flow is co- or counter-current and whether absorption or
289 desorption occurs. All four combinations which are possible in principle are summarized in
290 Figure 2, although no data are available for co-current desorption. Note that for absorption
291 the CO₂ is supplied mainly in the gas phase, while a smaller preloading of the liquid phase is
292 optional. For desorption in contrast, the CO₂ is supplied mainly in the liquid phase, while a
293 smaller preloading of the gas phase is optional. A detailed description is as follows.

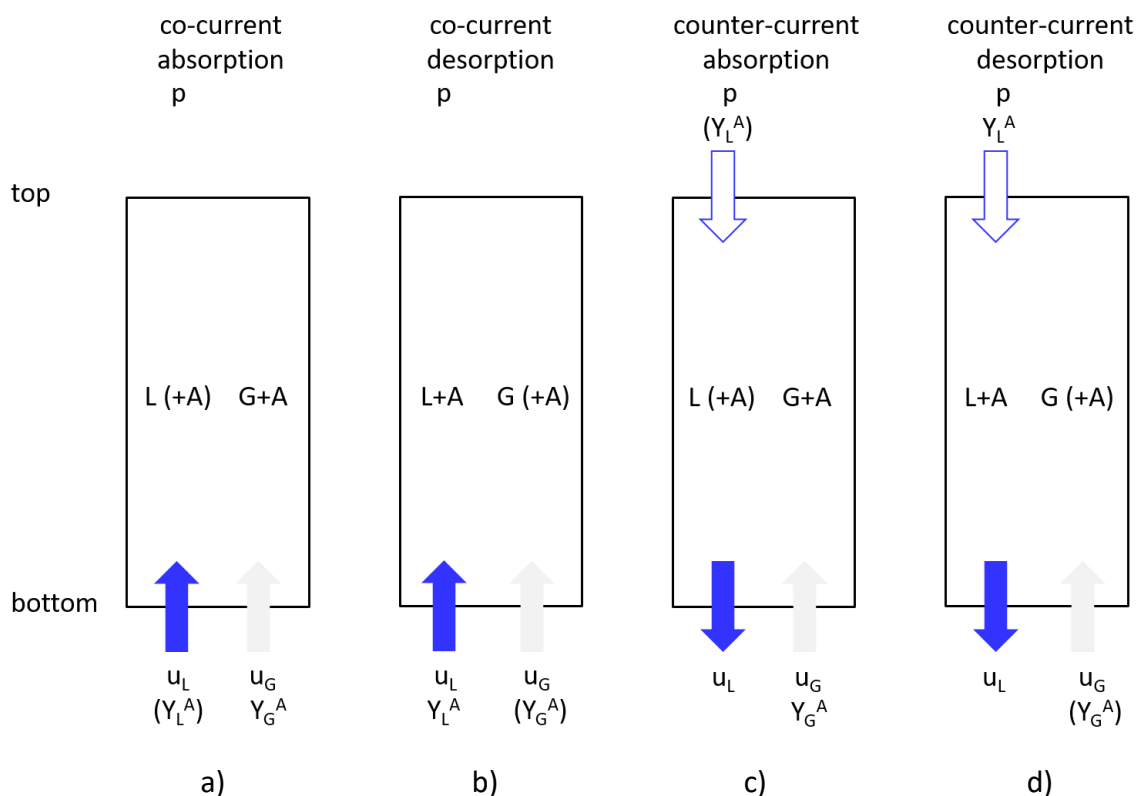
294 For the fluid dynamic variables, inlet conditions are imposed at the bottom of the column.
295 This inlet is modeled as a single homogeneous region where a mixture of gas and liquid at the
296 phase fraction given in Table 1 exists. The liquid and gas velocities are assumed uniform over

297 the cross-section and set to obtain the desired volume flow rate as given in Table 1. The flow
 298 direction is pointing into the domain for co-current flow and out of the domain for counter-
 299 current flow. At the top of the column, atmospheric pressure is imposed together with
 300 vanishing tangential velocity components and a vanishing normal derivative of gas fraction as
 301 an outlet condition.

302 For the turbulent variables following the work of Rzehak and Kriebitzsch (2015), a turbulent
 303 intensity of 5% and a turbulent length scale of $0.1 D$ are imposed at the bottom while a
 304 vanishing normal derivative is imposed at the top. This has been done independently of the
 305 flow direction, since these conditions are established for singlephase flow, which exists only
 306 at the bottom of the column. At the top in contrast, effects of bubble-induced turbulence
 307 would have to be considered.

308 For the mass fractions a specified value is prescribed for the gas phase at the bottom of the
 309 column, while a vanishing normal derivative is imposed at the top of the column. For the liquid
 310 phase mass fraction, a prescribed value is used at the bottom of the column for co-current
 311 flow and at the top of the column for counter-current flow. A vanishing normal derivative is
 312 imposed at the other location. Values for the mass fractions for each test case are given in
 313 Table 1.

314



317 Figure 2: Graphical summary of imposed boundary conditions for various configurations.
 318 Necessary addition of the transferred species (A) to gas (G) or liquid (L) phase is indicated by
 319 “+A”, optional preloading of the other phase by enclosing braces “()”.

320

321 Velocity boundary conditions on solid walls are no-slip for the liquid and free slip for the gas
322 phase. The latter assumes that direct contacts between the bubbles and the walls are
323 negligible. To avoid the need to resolve the viscous boundary layer, a single phase turbulent
324 wall function for a smooth wall is applied. Concentration boundary conditions on
325 impermeable walls are vanishing mass fractions, i.e. $Y_G^A = Y_L^A = 0$.

326

327 4 RESULTS AND DISCUSSION

328 All simulations are run with the *multiPhaseEulerFoam* solver of version 9 of the foundation
329 release of OpenFOAM (OpenFOAM Foundation 2021) using the models described in Section
330 3 and the parameters for each test case given in Table 1 of Section 2. All simulations were run
331 until a steady state was achieved. Axial profiles of gas fraction α_G and concentration of CO₂ in
332 gas or liquid $Y_G^{CO_2}$ or $Y_L^{CO_2}$ are considered and to this end cross-sectionally averaged values
333 are extracted from the simulation data. The scaled vertical coordinate y/H is used
334 throughout.

335 The simulation results are presented in three subsections. The first, subsection 4.1, considers
336 a case with co-current absorption in BC II. For this case, in addition to the experimental results
337 from Decker et al. (1978), comparison is also made to the previous simulations from Rzehak
338 and Krepper (2016) using ANSYS CFX. Subsection 4.2 studies a total of four cases in BC I, which
339 present a variety of configurations with co- and counter-current flow and absorption as well
340 as desorption. Finally in subsection 4.3, a demonstration of a polydisperse simulation taking
341 into account the shrinkage of the bubble during the absorption is given for the parameters of
342 case 16 in BC II again.

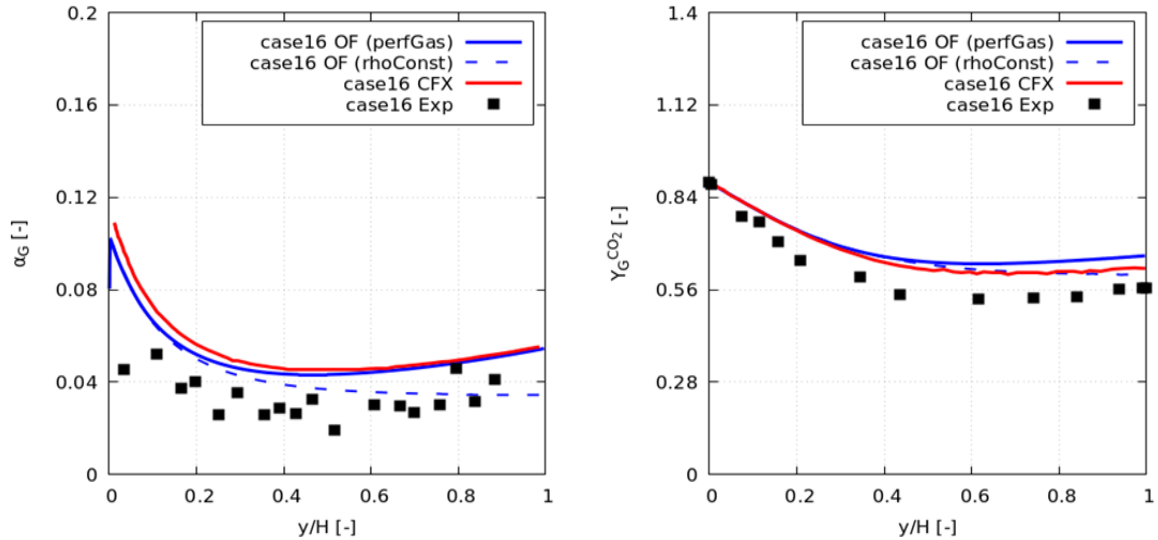
343

344 4.1 Comparison to previous simulations

345 Test case 16 in BC II (see Section 2), affords the possibility to make comparison of the present
346 simulation results obtained using OpenFOAM with those of a previous simulation carried out
347 in ANSYS CFX (Rzehak and Krepper 2016) in addition to the experimental data. Moreover, for
348 the OpenFOAM simulations comparison is made between two equations of state for the gas
349 phase, namely a perfect gas following the ideal gas law and an incompressible gas for which
350 the density is constant as described in Section 3.4. The earlier simulations using ANSYS CFX
351 were based exclusively on the ideal gas law. This test case is concerned with co-current
352 absorption, for which the inlet and outlet conditions are summarized in part a) of Figure 2.
353 Specifically, both liquid and gas enter at the column bottom with flow rates and
354 concentrations corresponding to the values used in the experiment (see Table 1). The results
355 obtained for this case are shown in Figure 3.

356 As seen in Figure 3 results of the present OpenFOAM simulation (blue lines) agree very closely
357 with those of the previous CFX simulation (red lines) for both the gas fraction α_G (left panel)
358 and the CO₂ mass fraction $Y_G^{CO_2}$ in the gas phase (right panel). The slight observed differences
359 between both simulations can be attributed to the different numerical methods employed.

360



361

362 Figure 3: Results for case 16 in BC II with co-current absorption. Left: gas fraction, α_G ; right:
 363 CO₂ mass fraction in the gas phase, $Y_G^{CO_2}$. Symbols: measurements from Deckwer et al. (1978);
 364 red lines: simulation results from Rzehak and Krepper (2016) using ANSYS CFX; blue lines:
 365 present simulation results using OpenFOAM; solid lines: results using the ideal gas equation
 366 of state for the gas; dashed lines: treating the gas as incompressible with constant density.

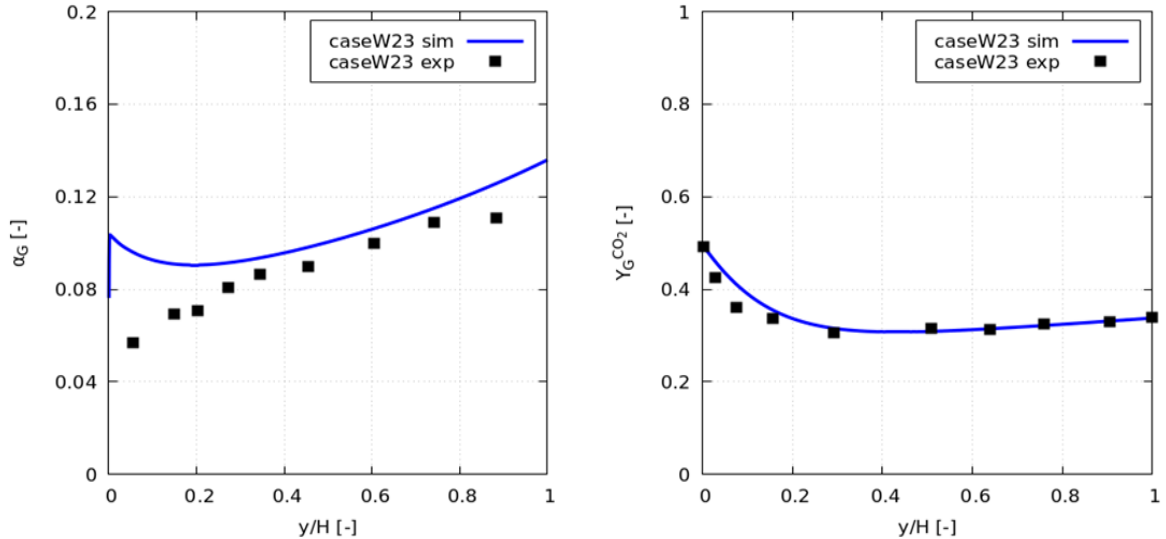
367 In comparison to the experimental results (symbols), the simulations overestimate both the
 368 gas fraction and the CO₂ mass fraction. Near the inlet below $y/H \lesssim 0.1$, the simulations
 369 predict a significantly higher gas fraction than observed in the experiment. As already
 370 discussed in detail by Rzehak and Krepper (2016), this is likely due to the simplified modelling
 371 of the inlet as a homogeneously mixed region, but since only a single experimental data point
 372 is available in this region, a clear judgement cannot be made. The jump right next to the inlet
 373 is most probably due to the approximate estimation of the gas fraction used for the inlet
 374 condition. In the upper part of the column for $y/H \gtrsim 0.1$, the agreement for the gas fractions
 375 is reasonable considering assumptions made in the model such as the neglect of bubble
 376 coalescence and breakup processes. The same also holds for the agreement between
 377 simulated and measured CO₂ mass fractions over the entire height of the column.

378 It may be noted that both the gas fraction and the CO₂ mass fraction in the gas phase decrease
 379 from the inlet up to $y/H \approx 0.5$ as expected due to the absorption of gas into the liquid.
 380 However, at this height equilibrium is reached between the CO₂ concentrations in both
 381 phases such that the mass source in Eq. (5) vanishes. With further increasing height, this
 382 equilibrium shifts towards a higher CO₂ content in the gas phase due to the decreasing
 383 hydrostatic pressure, which by the ideal gas law also reduces the gas density. This changes
 384 the direction of the mass transfer from absorption to desorption which is seen by the non-
 385 monotonic behavior of the curves in the plot. This feature had already been discussed in the
 386 experimental work of Deckwer et al. (1978) and is well reproduced by the simulations.
 387 Comparing results applying the ideal gas law (solid lines) to those taking the gas density as
 388 constant (dashed lines), it is seen that the non-monotonic behavior is absent in the latter,
 389 which corroborates the decrease of hydrostatic pressure and associated change in gas density
 390 as the pertinent mechanism.

391 4.2 New results for various configurations

392 Test cases W23, W13, W15, W3 in BC I (see Table 1 in Section 2) afford the possibility to study
393 a number of configurations with different boundary conditions that have not yet been
394 explored by Euler-Euler simulations including mass transfer. All simulations in this section
395 apply the ideal gas law for the gas phase.

396



397

398 Figure 4: Results for case W23 in BC I with co-current absorption. Left: gas fraction, α_G ; right:
399 CO₂ mass fraction in the gas phase, $Y_G^{CO_2}$. Symbols: measurements from Deckwer et al. (1978);
400 solid lines: present simulation results using OpenFOAM.

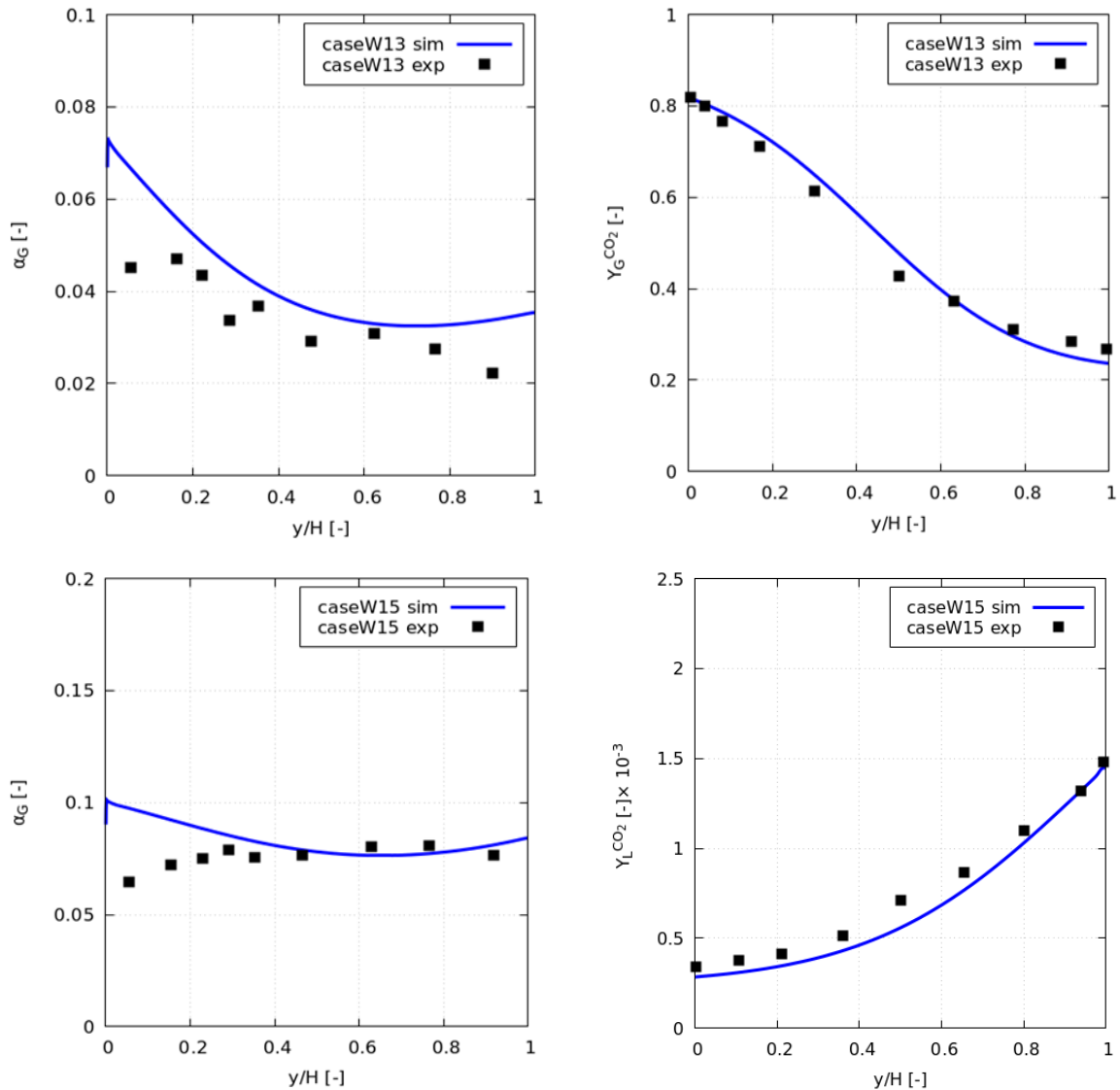
401 Like case 16 considered in the previous section 4.1, test case W23 is again concerned with
402 with co-current absorption with inlet and outlet conditions as summarized in part a) of Figure
403 2, but now the geometry is that of the larger column BC I. Results for this case are shown in
404 Figure 4.

405 While the agreement between simulations results (lines) and experimental data (symbols) is
406 even better than for case 16 for the CO₂ mass fraction in the gas phase (right panel), there
407 are more significant deviations for the gas fraction (left panel). Near the inlet there is a similar
408 overprediction of the gas fraction as found for case 16, which however here extends over a
409 larger portion of the column height and leads to a qualitatively different shape of the profile
410 in comparison with the measured data. While the simulations still show a non-monotonic
411 behavior as explained in the previous section, the experimental profile now is monotonically
412 increasing despite the fact that the bubbles loose mass. Possibly the homogeneous inlet
413 model used in the simulations describes the cross-shaped sparger used in BC I less well than
414 the porous plate one in BC II. In the upper half of the column the agreement between
415 simulations and experiment is rather good again.

416 Two further test cases W13 and W15 are available in BC I with counter-current absorption. In
417 this case the gas enters the column at the bottom, but the liquid is supplied from its top as
418 shown in Figure 2 c). The CO₂ is supplied mainly via the gas phase but the liquid is preloaded
419 by a certain amount of CO₂ for both of these cases. Results are shown in Figure 5. Note that

420 for case W13 in the top row, as before the CO₂ mass fraction in the gas phase $Y_G^{CO_2}$ was
 421 measured, but for case W15 in the bottom row, the CO₂ mass fraction in the liquid phase $Y_L^{CO_2}$
 422 is available.

423

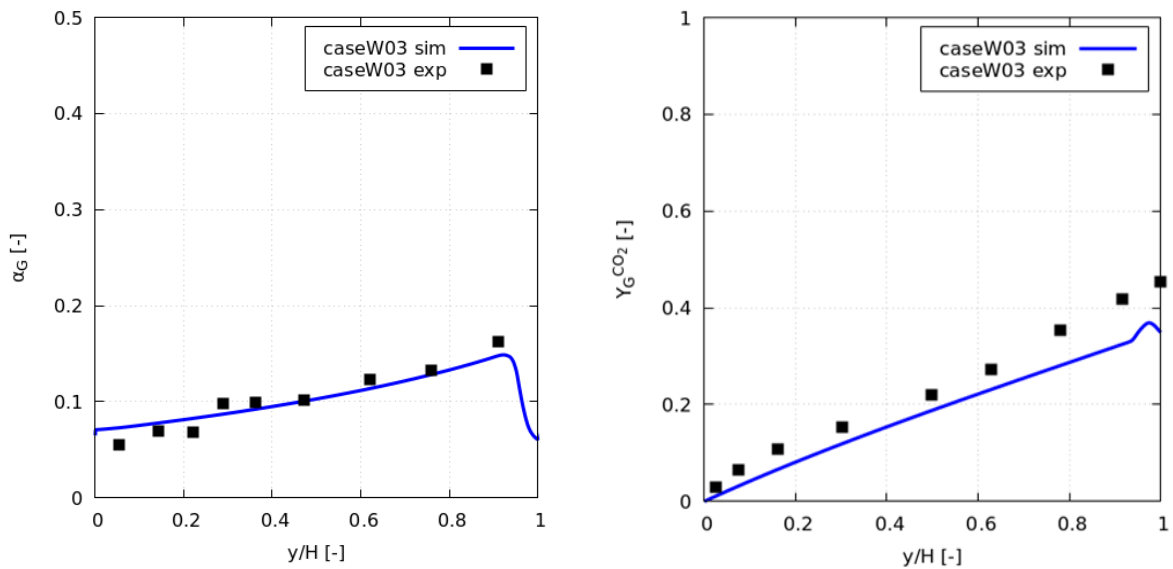


424 Figure 5: Results for cases W13 (top) and W15 (bottom) in BC I with counter-current
 425 absorption. Left: gas fraction, α_G ; right: CO₂ mass fraction in the gas phase, $Y_G^{CO_2}$, for case
 426 W13 and in the liquid phase, $Y_L^{CO_2}$, for case W15. Symbols: measurements from Deckwer et
 427 al. (1978); solid lines: present simulation results using OpenFOAM.

428 As seen by comparing Figure 5 to Figure 4 the overall trends for counter-current absorption
 429 are the same as for co-current absorption. The agreement between simulation and
 430 experiment is quite good for the CO₂ mass fractions (right column), which here includes the
 431 one in the liquid (for case W15) in addition to that in the gas (for case W13). Concerning the
 432 gas fraction (left column) the same pattern observed previously reappears for both cases: The
 433 simulated values overestimate the measured ones in some region near the inlet while
 434 providing a reasonable agreement in the upper part of the column. Also the nonmonotonic
 435 shape of the profile persists in the simulations while the measured profiles are monotonously

436 decreasing for case W13 or feature a rather constant value over a certain height range for
437 case W15. The same possible explanation given for case W23 applies here as well.

438 Finally, there is also one test case in BC I with counter-current desorption, namely case W03.
439 As for the previous counter-current absorption cases, the gas enters the column at the
440 bottom while the liquid is supplied from its top. However, now the CO₂ is supplied via the
441 liquid phase as shown in Figure 2 d) and there is no preloading of the gas. Results for this case
442 are shown in Figure 6.



443
444 Figure 6: Results for case W03 in BC I with counter-current desorption. Left: gas fraction, α_G ;
445 right: CO₂ mass fraction in the gas phase, $Y_G^{CO_2}$. Symbols: measurements from Deckwer et al.
446 (1978); solid lines: present simulation results using OpenFOAM.

447 In this case, for both the profiles of gas fraction and of CO₂ mass fraction in the gas phase very
448 good agreement between simulation and experiment is found. For this configuration, the
449 bubbles on their rise through the column are exposed to an increasing concentration of CO₂
450 in the liquid, hence the desorption process leads to a corresponding increase in the CO₂
451 concentration of the gas as well as the gas fraction over the column height. The drop in gas
452 fraction near the top boundary is likely caused by the imposed outlet conditions, which like
453 the condition at the inlet may not provide an accurate reflection of the true experimental
454 setup. Hence, this feature of the simulations may or may not correspond with reality, a clear
455 judgement being impossible due to a lack of measurement points close enough to the outlet.

456
457
458

459 4.3 Demonstration of bubble shrinkage

460 The present section demonstrates how the shrinking of bubbles due to absorption can be
461 captured by the class method implemented in OpenFOAM. The parameters of the
462 demonstration case are chosen similar to those of case 16 in BC II of Deckwer et al (1978).
463 Since there are no measurements of the axial evolution of the bubble size in that work,
464 comparison is made between the polydisperse simulation based on the class method and two
465 monodisperse simulations, the first using the same bubble size as the initial value of the
466 polydisperse simulation ($d_B = 2.9$ mm) and the second one using the same bubble size as the
467 final value of the polydisperse simulation ($d_B = 1.9$ mm). For the mass transfer coefficient,
468 the correlation of Brauer (1979) is used, i.e. $Sh = (2 + 0.015 Re^{0.89} Sc^{0.7})$, where Sh , Re and
469 Sc denote the dimensionless Sherwood, Reynolds, and Schmidt numbers. The gas density was
470 kept constant in these simulations to bring out the crossover of the polydisperse simulations
471 between the two monodisperse ones more clearly. The results are shown in Figure 7 and
472 Figure 8.

473 The top part of Figure 7 shows the axial evolution of the bubble size in the polydisperse
474 simulation for different numerical setups. The size range from 0 to 4 mm was discretized in
475 size groups of uniform width Δd . The solid lines are for simulations using 40 size groups, the
476 dotted ones for 20 size groups. A slight influence of the number of size groups is visible in the
477 upper part of the column. Also the blue lines are for an inlet bubble size distribution with all
478 bubbles concentrated in a single size group, i.e. given by a δ -function, while for the red lines,
479 the inlet distribution was a Gaussian with full width at half maximum of ~ 2 mm. Again a slight
480 influence of the different inlet distribution is visible in the upper part of the column.

481 The middle and bottom part of Figure 7 show the axial evolution bubble size distribution,
482 where each curve corresponds to a different axial coordinate as indicated in the legend. The
483 number of size groups was 40 for both cases, but the middle part is for the δ -function inlet
484 distribution, while the bottom part is for the Gaussian inlet distribution. For the δ -function
485 inlet distribution the diffusive nature of the applied upwind-type discretization of the mass
486 transfer between size groups (see Section 3.3) is obvious in the significant spreading of the
487 width of the distribution which eventually develops into a Gaussian form. For the Gaussian
488 inlet distribution the width has been chosen such that no further spreading occurs. In this
489 case, it is seen that the evolution becomes a simple shift of the entire distribution.

490 Overall, the mean bubble size can be represented well by the simulations, the effect of the
491 different numerical settings being negligible for practical purposes. The shape of the obtained
492 distributions is largely determined by numerical diffusion and should not be taken to
493 represent reality. As long as mass transfer is the only process that changes the bubble size,
494 this is not a severe drawback, but if bubble coalescence and breakup processes should be
495 included as well, an improved numerical method for the shrinkage and growth due to mass
496 transfer would be desirable to avoid the numerical diffusion.

497

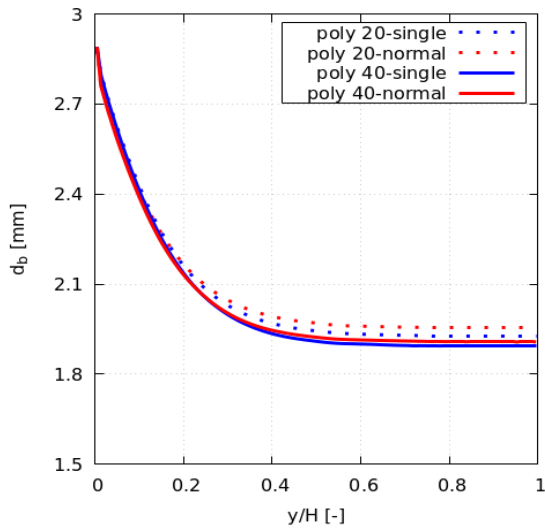
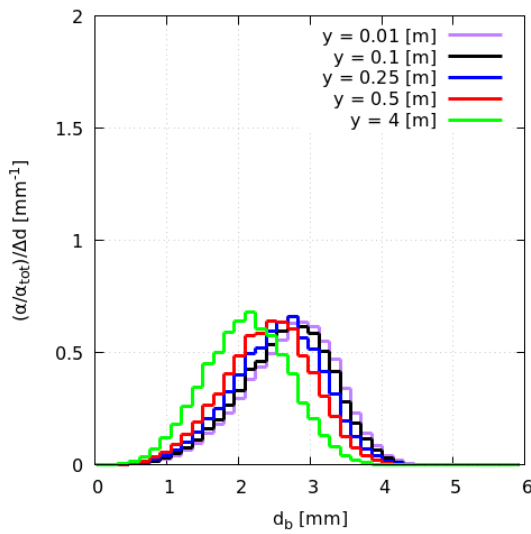
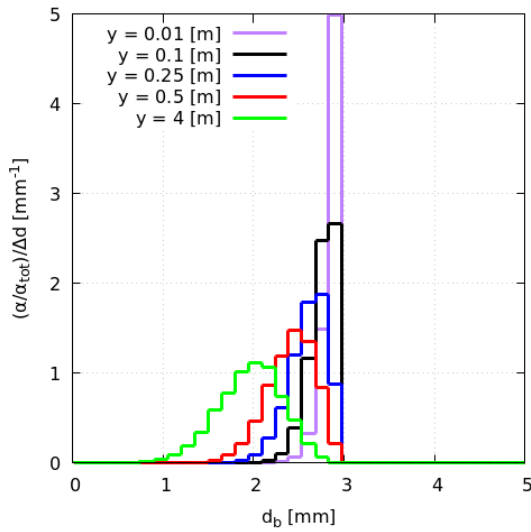


Figure 7: Axial evolution of bubble size for case 16 in BC II with co-current absorption in present simulations using OpenFOAM. Top: mean bubble size d_B with solid lines: simulation using 40 size groups, dotted lines: simulation using 20 size groups, blue lines: δ -function inlet distribution, red lines: Gaussian inlet distribution. Middle: bubble size distributions at different axial locations for 40 size groups and δ -function inlet distribution. Bottom: bubble size distributions at different axial locations for 40 size groups and Gaussian inlet distribution.



498

499

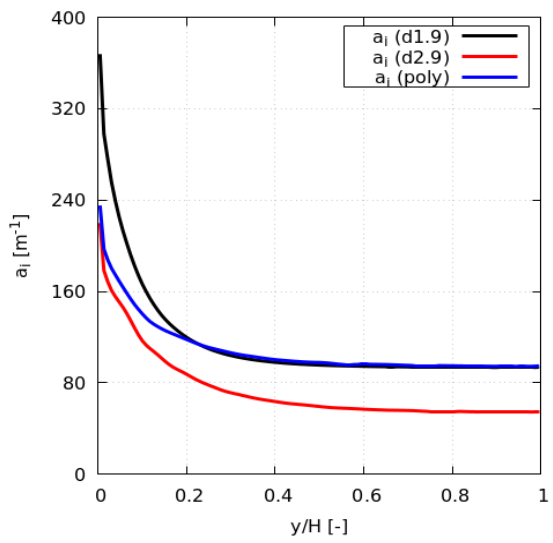
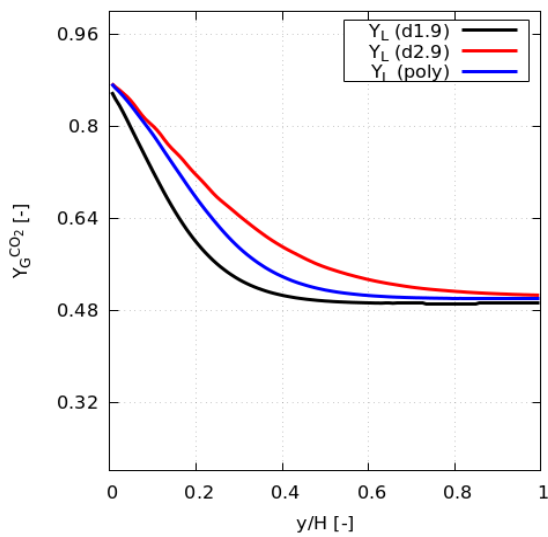
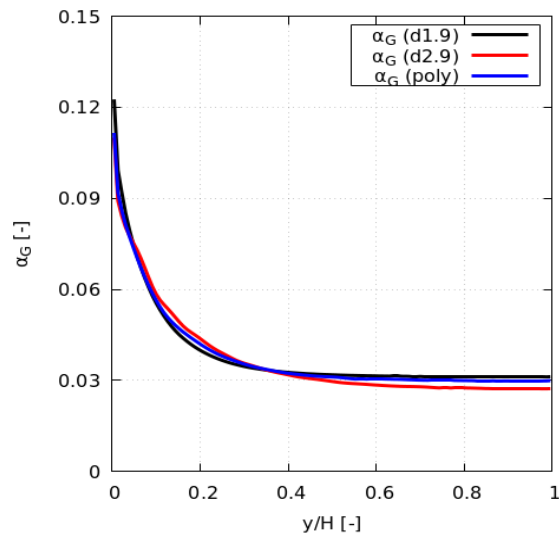


Figure 8: Effects of polydispersity for case 16 in BC II with co-current absorption in present simulations using OpenFOAM. Top: interfacial area concentration a_i ; Middle: gas fraction, α_G ; Bottom: CO_2 mass fraction in the gas phase, $Y_L^{\text{CO}_2}$. Blue lines: polydisperse simulation; red lines: monodisperse simulation at initial bubble size $d_B = 2.9$ mm; black lines: monodisperse simulation at final bubble size $d_B = 1.9$ mm.



502 Figure 8 shows the axial evolution of the interfacial area concentration (top), gas fraction
503 (middle) and CO₂ mass fraction in the gas (bottom). In all of these, the red curve gives the
504 result of the monodisperse simulation with $d_B = 2.9$ mm, which is the same as already
505 presented in Section 4.1. The black curve gives the result of the monodisperse simulation with
506 $d_B = 1.9$ mm and the blue curve that of a polydisperse simulation with 40 size classes and a
507 δ -function inlet size distribution. For the interfacial area concentration and the CO₂ mass
508 fraction in the gas the expected crossover of results of the polydisperse simulation between
509 the two monodisperse ones is evident. For the gas fraction, the results of all three simulations
510 are too close together to clearly display the crossover. Overall the polydisperse simulation
511 results show a plausible behavior with respect to the two monodisperse ones. On the basis of
512 the data available in the work of Deckwer et al (1978), this is the best achievable conclusion
513 to indicate the performance of the present OpenFOAM implementation. A full validation of
514 this approach by comparison with actual measurements of the bubble size will be pursued in
515 the future.

516

517 5 SUMMARY AND CONCLUSIONS

518 Mass transfer in bubble columns with different boundary conditions comprising absorption
519 and desorption as well as co- and counter-current flow has been studied by means of Euler-
520 Euler simulations. A recent version of the open-source software OpenFOAM has been
521 qualified for that purpose including an implementation of the class-method to solve the
522 population-balance equation. Available data from the literature for the different boundary
523 conditions have been used for comparison.

524 Comparison between the present simulation results and previous simulations using ANSYS
525 CFX based on the same models confirms the validity of the implementation of mass-transfer
526 in OpenFOAMs *mutiPhaseEulerFoam* solver.

527 Overall, the agreement between simulation and experimental results is reasonable within the
528 approximations made in the modeling. This confirms and extends the findings from previous
529 work on absorption in co-current flow to a variety of other configurations. The simplified
530 modeling of the inlet as a homogeneous region appears to be the major cause for deviations
531 in the gas fraction profiles near the inlet. Unfortunately, the experimental resolution in this
532 region is often less than desirable and the detailed geometric information to improve the inlet
533 modeling is often lacking in experimental work (see e.g. Hillmer 1993, Shirzadi 2012).
534 Somewhat surprisingly, the CO₂ mass fractions are not severely affected and good agreement
535 is found over the entire column height.

536 Of course, the assumptions of a fixed monodisperse bubble size distribution and the use of
537 the experimentally determined values for the mass transfer coefficient limit the predictive
538 capability of the model. However in view of the limitations of the presently used dataset and
539 the still active research on suitable models for both the mass transfer coefficient and
540 coalescence and breakup rates, improving on these assumptions must be left for future work.
541 Experimental data with measured bubble size distributions at several heights of the column
542 in addition to concentration of transferred species, ideally in both phases, and gas fraction
543 would be very desirable in order to proceed in this direction.

544 Nonetheless, the necessary framework by means of a class method for the population balance
545 equation has already been implemented and tested by showing that it produces a crossover

546 between two monodisperse simulations as expected. Likewise independence of the results
 547 from numerical settings such as the number of classes used to discretize the bubble size
 548 distribution could be shown.

549

550 6 ACKNOWLEDGEMENT

551 This work has been carried out in the frame of a research project (GZ: RZ 11/3-1) funded by
 552 the DFG.

553

554 7 NOMENCLATURE

Latin Formula Characters

Symbol	Description	Unit	Symbol	Description	Unit
a_I	interfacial area concentration	m^{-1}	R	universal gas constant	$J K^{-1} mol^{-1}$
c	molar concentration	$mol m^{-3}$	Re	Reynolds number	-
d_B	bubble diameter	m	Sc	Schmidt number	-
D	lateral dimension	m	Sh	Sherwood number	-
D	diffusion coefficient	$m^2 s^{-1}$	t	time	s
F	force per unit volume	$N m^{-3}$	T	temperature	$^{\circ}C, K$
g	acceleration of gravity	$m s^{-2}$	\mathbf{T}	stress tensor	$N m^{-2}$
H	axial dimension	m	\mathbf{u}	mean velocity	$m s^{-1}$
He	Henry constant	-	\mathbf{u}'	fluctuating velocity	$m s^{-1}$
J	superficial velocity = volumetric flux	$m s^{-1}$	W	spanwise dimension	m
k	mass transfer coefficient	$m s^{-1}$	x	lateral coordinate	m
k	specific turbulent kinetic energy	$m^2 s^{-2}$	X	mole fraction	-
m	mass	-	y	axial coordinate	m
M	molar mass	-	Y	mass fraction	-
p	pressure	Pa	z	spanwise coordinate	m
r	radial coordinate	m			

555

Greek Formula Characters

Symbol	Description	Unit	Symbol	Description	Unit
α	phase fraction	-	ρ	density, mass concentration	$kg m^{-3}$
ϵ	turbulent dissipation rate	$m^2 s^{-3}$	σ	surface tension	$N m^{-1}$

Γ	source term due to mass transfer in species equation	$\text{kg m}^{-3} \text{s}^{-1}$	ϕ	source term due to mass transfer in momentum equation	N m^{-3}
μ	dynamic viscosity	Pa s	Ψ	source term due to mass transfer in continuity equation	$\text{kg m}^{-3} \text{s}^{-1}$
ν	kinematic viscosity	$\text{m}^2 \text{s}^{-1}$	ω	turbulent frequency	s^{-1}

556

Indices and Abbreviations

Symbol	Description	Symbol	Description
A	of transferred species	H_2O	of water
abs.	absorption	L	liquid phase
bot	at bottom	mol	molecular
CO_2	of carbon dioxide	top	at top
des.	desorption	turb	turbulent
eff	effective	X	of any species
G	gas phase		

557

558 8 REFERENCES

- 559 Brauer, H., 1979. Particle / fluid transport processes. *Progress in Chemical Engineering* 17, 61–
560 99.
- 561 Brauer, H., 1981. Mass transfer operations between liquid films and adjoining gas streams.
562 *Progress in Chemical Engineering* 19, 81–111.
- 563 Burckhart, R., 1976. Stofftransport in hohen Blasensäulen. PhD-thesis, *TU Berlin* (in German).
- 564 Burns, A. D., Frank, T., Hamill, I., Shi, J.-M., 2004. The Favre averaged drag model for
565 turbulence dispersion in Eulerian multi-phase flows. *Proc. 5th Int. Conf. on Multiphase Flow*,
566 ICMF2004, Yokohama, Japan.
- 567 Cockx, A., Do-Quang, Z., Audic, J., Line, A. and Roustan, M., 2001. Global and local mass
568 transfer coefficients in waste water treatment process by computational fluid dynamics.
569 *Chemical Engineering and Processing: Process Intensification* 40, 187–194.
- 570 Deckwer, W.-D., Adler, I. and Zaidi, A., 1978. A comprehensive study on CO_2 -interphase mass
571 transfer in vertical cocurrent and countercurrent gas-liquid flow. *Canadian Journal of*
572 *Chemical Engineering* 56, 43–55.
- 573 Drew, D. A., Passman, S. L., 1998. Theory of Multicomponent Fluids, *Springer*.
- 574 Hillmer, G., 1993. Experimentelle Untersuchung und fluiddynamische Modellierung von
575 Suspensionsblasensäulen. Univ. Erlangen-Nuernberg.
- 576 Hlawitschka, M. W., Oßberger, M., Backes, C., Klüfers, P., and Bart, H.-J., 2017a. Reactive mass
577 transfer of single NO bubbles and bubble bouncing in aqueous ferric solutions – A feasibility
578 study. *Oil & Gas Science and Technology* 72, 11.

579 Hlawitschka, M., Kovats, P., Zähringer, K., and Bart, H.-J. , 2017b. Simulation and experimental
580 validation of reactive bubble column reactors. *Chemical Engineering Science* 170, 306–319.

581 Hori, Y., Bothe, D., Hayashi, K., Hosokawa, S., and Tomiyama, A., 2020. Mass transfer from
582 single carbon-dioxide bubbles in surfactant-electrolyte mixed aqueous solutions in vertical
583 pipes. *International Journal of Multiphase Flow* 124, 103207.

584 Hosokawa, S., Tomiyama, A., Misaki, S. and Hamada, T., 2002. Lateral migration of single
585 bubbles due to the presence of wall. *Proc. ASME Joint U.S.-European Fluids Engineering
586 Division Conference, FEDSM2002*, Montreal, Canada.

587 Ishii, M. and Hibiki, T., 2011. Thermo-fluid dynamics of two-phase flow. *Springer*, 2nd ed.

588 Ishii, M. and Zuber, N., 1979. Drag coefficient and relative velocity in bubbly, droplet or
589 particulate flows. *AIChE Journal* 25, 843–855.

590 Kipping, R., Kryk, H., and Hampel, U., 2020. Experimental analysis of gas phase dynamics in a
591 lab scale bubble column operated with deionized water and NaOH solution under uniform
592 bubbly flow conditions. *Chemical Engineering Science* 229, 116056.

593 Kovats, P., Thevenin, D., and Zaehring, K., 2018. Characterizing fluid dynamics in a bubble
594 column aimed for the determination of reactive mass transfer. *Heat and Mass Transfer* 54,
595 453–461.

596 Krauß, M. and Rzehak, R., 2017. Reactive absorption of CO₂ in NaOH: Detailed study of
597 enhancement-factor models. *Chemical Engineering Science* 166, 193–209.

598 Krauß, M. and Rzehak, R., 2018. Reactive absorption of CO₂ in NaOH: An Euler-Euler
599 simulation study. *Chemical Engineering Science* 181, 199–214.

600 Krepper, E., Lucas, D., Frank, T., Prasser, H.-M. and Zwart, P., 2008. The inhomogeneous
601 MUSIG model for the simulation of polydispersed flows. *Nuclear Engineering and Design* 238,
602 1690–1702.

603 Lehnigk, R., 2020. A generalized population balance model for the simulation of polydisperse
604 multiphase flows within the Euler-Euler framework. PhD thesis Technical University Dresden.

605 Lehnigk, R., Bainbridge, W., Liao, Y., Lucas, D., Niemi, T., Peltola, J., Schlegel, F., 2022. An
606 open-source population balance modeling framework for the simulation of polydisperse
607 multiphase flows. *AIChE Journal* 68, e17539.

608 Liao, J., Ziegenhein, T., and Rzehak, R., 2016. Bubbly flow in an airlift column: a CFD study.
609 *Journal of Chemical Technology & Biotechnology* 91, 2904–2915.

610 Ma, T., Santarelli, C., Ziegenhein, T., Lucas, D., and Froehlich, J., 2017. Direct numerical
611 simulation-based Reynolds-averaged closure for bubble-induced turbulence. *Physical Review
612 Fluids* 2, 034301.

613 Marchisio, D. L. and Fox, R. O., 2013. Computational Models for Polydisperse Particulate and
614 Multiphase Systems. *Cambridge University Press*.

615 Menter, F. R., 2009. Review of the shear-stress transport turbulence model experience from
616 an industrial perspective. *International Journal of Computational Fluid Dynamics* 23, 305–316.

617 OpenFOAM Foundation, 2021. OpenFOAM v9 User Guide, OpenFOAM Foundation,
618 <https://cfd.direct/openfoam/user-guide>.

619 OpenFOAM Foundation, 2021a. [https://github.com/OpenFOAM/OpenFOAM-](https://github.com/OpenFOAM/OpenFOAM-dev/commit/1a3ae93fb372e1d49aac51e7bd0b9cbfc4ceb0b6)
620 [dev/commit/1a3ae93fb372e1d49aac51e7bd0b9cbfc4ceb0b6](https://github.com/OpenFOAM/OpenFOAM-dev/commit/1a3ae93fb372e1d49aac51e7bd0b9cbfc4ceb0b6) .

621 Parekh, J. and Rzehak, R., 2018. Euler-Euler multiphase CFD-simulation with full Reynolds
622 stress model and anisotropic bubble-induced turbulence. *International Journal of Multiphase*
623 *Flow* 99, 231–245.

624 Ramkrishna, D., 2000. Population Balances: Theory and Applications to Particulate Systems in
625 Engineering. *Academic Press*.

626 Rzehak, R. and Krepper, E., 2013. Bubble-induced turbulence: Comparison of CFD models.
627 *Nuclear Engineering and Design* 258, 57–65.

628 Rzehak, R. and Krepper, E., 2013a. CFD modeling of bubble-induced turbulence. *International*
629 *Journal of Multiphase Flow* 55, 138–155.

630 Rzehak, R. and Krepper, E., 2015. Bubbly flows with fixed polydispersity: Validation of a
631 baseline closure model. *Nuclear Engineering and Design* 287, 108–118.

632 Rzehak, R. and Kriebitzsch, S., 2015. Multiphase CFD-simulation of bubbly pipe flow: A code
633 comparison. *International Journal of Multiphase Flow* 68, 135–152.

634 Rzehak, R., Krepper, E., Liao, Y., Ziegenhein, T., Kriebitzsch, S. and Lucas, D., 2015. Baseline
635 model for the simulation of bubbly flows. *Chemical Engineering and Technology* 38, 1972–
636 1978.

637 Rzehak, R., Krepper, E., 2016. Euler-Euler simulation of mass-transfer in bubbly flows.
638 *Chemical Engineering Science* 155, 459–568.

639 Rzehak, R. 2016. Modeling of mass-transfer in bubbly flows encompassing different
640 mechanisms. *Chemical Engineering Science* 151, 139–143.

641 Rzehak, R., Ziegenhein, T., Kriebitzsch, S., Krepper, E., and Lucas, D., 2017.
642 Unified modeling of bubbly flows in pipes, bubble columns, and airlift columns.
643 *Chemical Engineering Science* 157, 147–158.

644 Rzehak, R., Krauß, M., Kovats, P., and Zähringer, K., 2017a. Fluid dynamics in a bubble column:
645 New experiments and simulations. *International Journal of Multiphase Flow* 89, 299–312.

646 Shi, P. and Rzehak, R., 2018. Bubbly flow in stirred tanks: Euler-Euler / RANS modeling.
647 *Chemical Engineering Science* 190, 419–435.

648 Solsvik, J., 2018. Lagrangian modeling of mass transfer from a single bubble rising in stagnant
649 liquid. *Chemical Engineering Science* 190, 370–383.

650 Shirzadi, H., 2012. An experimental and computational study of hydrodynamics and mass
651 transfer in gas-liquid bubble columns. PhD thesis Univ. Paderborn.

652 Taborda, M. A. and Sommerfeld, M., 2021. Reactive LES-Euler/Lagrange modelling of bubble
653 columns considering effects of bubble dynamics. *Chemical Engineering Journal* 407, 127222.

654 Tomiyama, A., Kataoka, I., Zun, I., and Sakaguchi, T., 1998. Drag coefficients of single bubbles
655 under normal and micro gravity conditions. *JSME International Journal B* 41, 472–479.

- 656 Tomiyama, A., Tamai, H., Zun, I., and Hosokawa, S., 2002. Transverse migration of single
657 bubbles in simple shear flows. *Chemical Engineering Science* 57, 1849–1858.
- 658 Yeoh, G. H. and Tu, J. Y., 2010. Computational Techniques for Multiphase Flows — Basics and
659 Applications, *Butterworth-Heinemann*.
- 660 Zhang, C., Yuan, X., Luo, Y., and Yu, G., 2018. Prediction of species concentration distribution
661 using a rigorous turbulent mass diffusivity model for bubble column reactor simulation part I:
662 Application to chemisorption process of CO₂ into NaOH solution. *Chemical Engineering
663 Science* 184, 161–171.
- 664 Ziegenhein, T., Rzehak, R., Krepper, E. and Lucas, D., 2013. Numerical simulation of
665 polydispersed flow in bubble-columns with the inhomogeneous multi-size-group model.
666 *Chemie Ingenieur Technik* 85, 1080–1091.
- 667 Ziegenhein, T., Rzehak, R., Ma, T., and Lucas, D., 2017. A unified approach for modeling
668 uniform and non-uniform bubbly flows. *Canadian Journal of Chemical Engineering* 95, 170–
669 179.
- 670